Materials Science-Poland
http://www.materialsscience.pwr.wroc.pl/
DOI: 10.2478/msp-2019-0083

Stereometric analysis of Ta_2O_5 thin films

DINARA SOBOLA[1], PAVEL KASPAR[1,*], JINDRICH OULEHLA[1], ŞTEFAN ŢĂLU[2], NIKOLA PAPEŽ[1]

[1]Brno University of Technology, Faculty of Electrical Engineering and Communication, Physics Department, Technická 8, 616 00 Brno, Czech Republic

[2]Technical University of Cluj-Napoca, The Directorate of Research, Development and Innovation Management (DMCDI), Constantin Daicoviciu Street, no. 15, Cluj-Napoca, 400020, Cluj county, Romania

The purpose of this work is the study of the correlation between the thickness of tantalum pentoxide thin films and their three-dimensional (3D) micromorphology. The samples were prepared on silicon substrates by electron beam evaporation. The differences in surface structure of the processed and reference samples were investigated. Compositional studies were performed by energy-dispersive X-ray spectroscopy. Stereometric analysis was carried out on the basis of atomic force microscopy (AFM) data, for tantalum pentoxide samples with 20 nm, 40 nm, 60 nm, 80 nm and 100 nm thicknesses. These methods are frequently used in describing experimental data of surface nanomorphology of Ta_2O_5. The results can be used to validate theoretical models for prediction or correlation of nanotexture surface parameters.

Keywords: *atomic force microscopy; stereometric analysis; Ta_2O_5, topography*

1. Introduction

Tantalum pentoxide (Ta_2O_5) finds use in many electrical and optical applications. In the electrical field it is often employed as a dielectric insulator in metal-insulator-metal (MIM) or metal-insulator-semiconductor (MIS) structures [1]. These devices are used for example in scaled-down versions of ultra-large scale integrated devices (ULSI), such as dynamic random access memory cards for computing, or three-dimensional capacitor structures, such as the trenched-type capacitor (TTC) [2]. Because of its properties Ta_2O_5 is also employed in integrated sensors for hydrogen ion sensing membranes or protein detection, making it sought after in the field of biological and biochemical sensors [3]. Tantalum pentoxide, due to its high refractive index and very low absorption coefficient [4], is also suitable for the fabrication of thin films for the purposes of antireflective coatings for solar cells or CCD devices, and for protection of material surfaces against corrosion because of its high chemical stability [5]. Preparation of Ta_2O_5 has been a challenging issue, but there are a number of possible methods to create thin Ta_2O_5 layers, with varying degree of success and specific properties of the prepared layer. Some of the most often used methods are standard techniques of thin-film preparation, like chemical vapor deposition (CVD) or magnetron sputtering, but because of the chemical nature of Ta_2O_5, a more specialized processes, like pulse laser ablation or sol-gel method should be employed [6]. The possible uses of Ta_2O_5 are numerous, and the mentioned examples are only some of the better explored ones. Because of the wide variety of possible applications, the material properties of tantalum pentoxide are continuously explored. This paper investigates the changes of chemical composition and optical properties and also presents, so far only briefly explored stereometric analysis of Ta_2O_5 surfaces with the film thickness of 20 nm, 40 nm, 60 nm, 80 nm and 100 nm. Imaging by AFM can bring outstanding results in the field of nanostructured surface research and analysis, especially when thin films are concerned [7–11]. Interpretation of AFM results is usually reduced to plain surface description – roughness and peak-valley ratio, though. A comprehensive description of surface morphology of studied materials is an ongoing challenge necessary

*E-mail: kasparp@feec.vutbr.cz

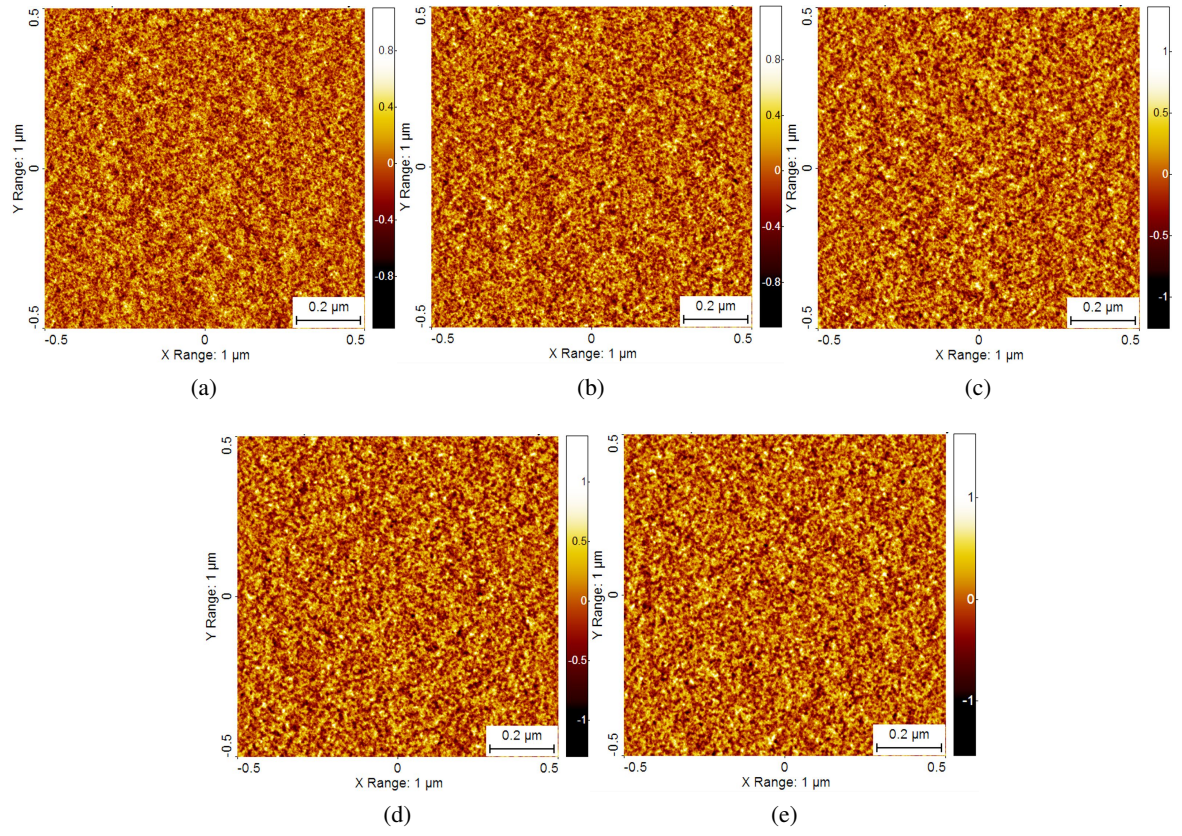

Fig. 1. 2-D AFM images of the surface microtexture of Ta_2O_5 of samples, for scanning square areas of 1 µm × 1 µm. Sample thickness: (a) 20 nm; (b) 40 nm; (c) 60 nm; (d) 80 nm; (e) 100 nm.

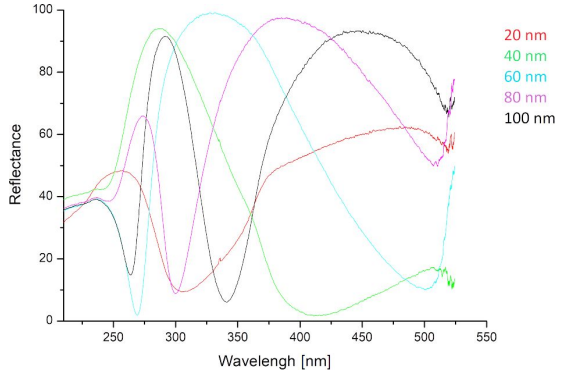

Fig. 2. Reflection spectra of Ta_2O_5 films.

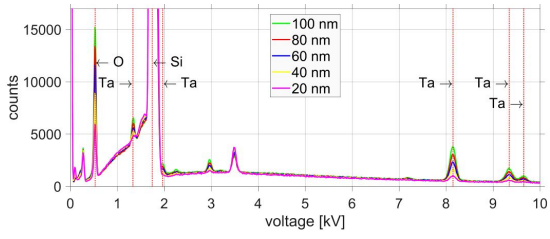

Fig. 3. EDX spectra of Ta_2O_5 films with different thicknesses.

for understanding their properties and their potential for technological exploitation [12–16]. In the presented work, the topography of Ta_2O_5 has been studied in correlation with film thickness. Structural and optical properties have been described using EDX and reflectometry spectra. For the 3D characterization of sample surface, AFM imaging has been used and a fractal analysis has been performed on the acquired data.

2. Materials and methods

Ta_2O_5 films grown by electron beam evaporation, were chosen for the experiment. Atomic force microscopy (AFM) characterization was

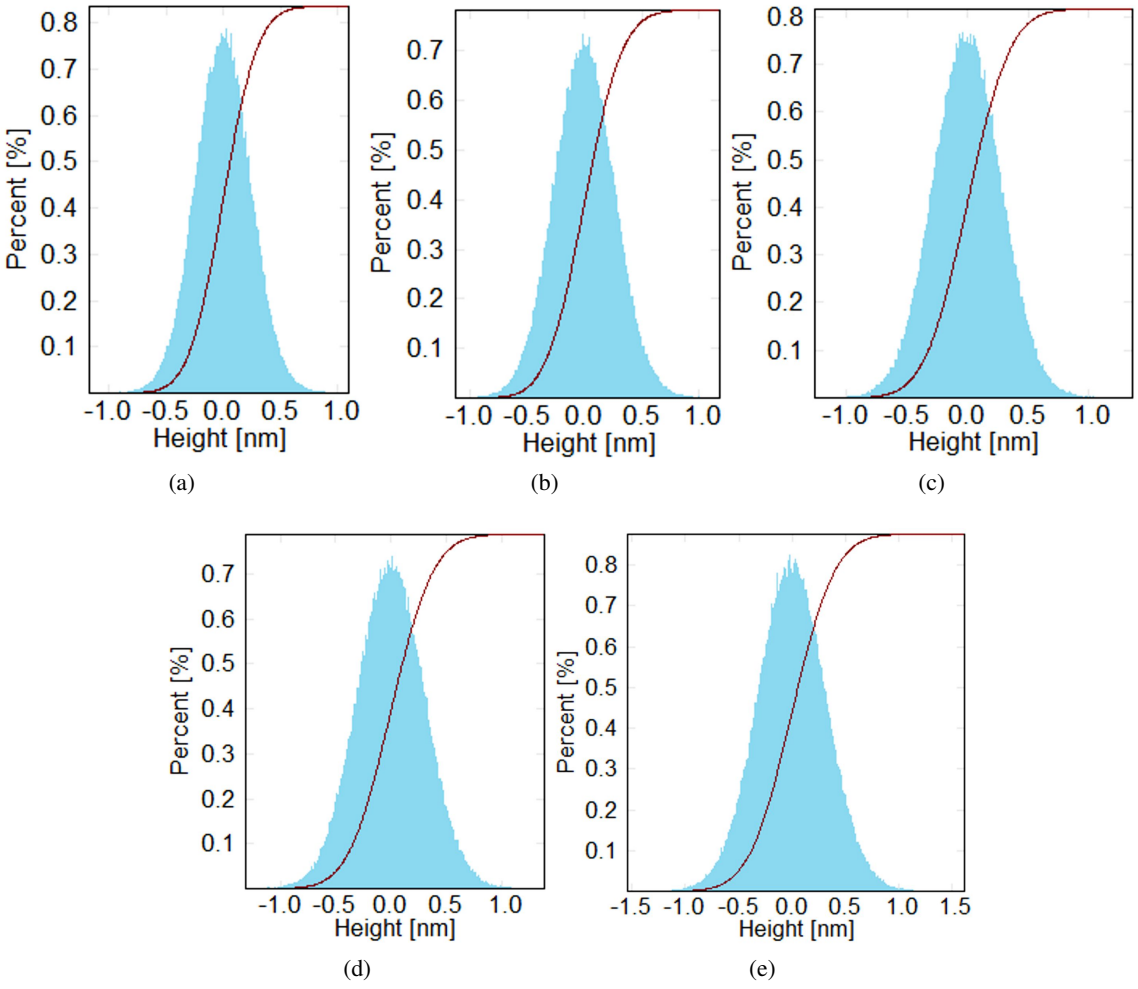

Fig. 4. Height distribution histogram with the integration curve of the histogram computed for images of Fig. 1. Sample thickness: (a) 20 nm; (b) 40 nm; (c) 60 nm; (d) 80 nm; (e) 100 nm.

carried out for the quantitative analysis of specific microstructural features of samples. Images of scanned square of 1 μm × 1 μm were chosen for further processing (Fig. 1). The scanning was carried out in tapping mode, at room temperature and normal humidity. The relevant 3-D AFM images of the Ta_2O_5 surface microtexture of samples with 20 nm, 40 nm, 60 nm, 80 nm and 100 nm thickness, obtained using AFM for a 1 μm × 1 μm square area are shown in Fig. 1a to Fig. 1e.

Fig. 2 shows reflectance spectra of the films after calibration on silicon standard. Shifting of maxima and minima is the result of the difference in the films thickness.

The depth of EDX analysis depends on parameters of electron beam and includes few microns of near-surface area. The spectra obtained at 20 keV electron beam are shown in Fig. 3.

3. Results and discussion

Pure imaging of surface topography in this case is insufficient and numerical processing is demanded for description of differences in the samples [17–22]. The stereometric analysis was carried out on the basis of AFM data, because it gives real 3D information about surface texture [23–28]. The surface topography was described in terms of stereometric analysis using the SPIP^{TM} 6.7.4

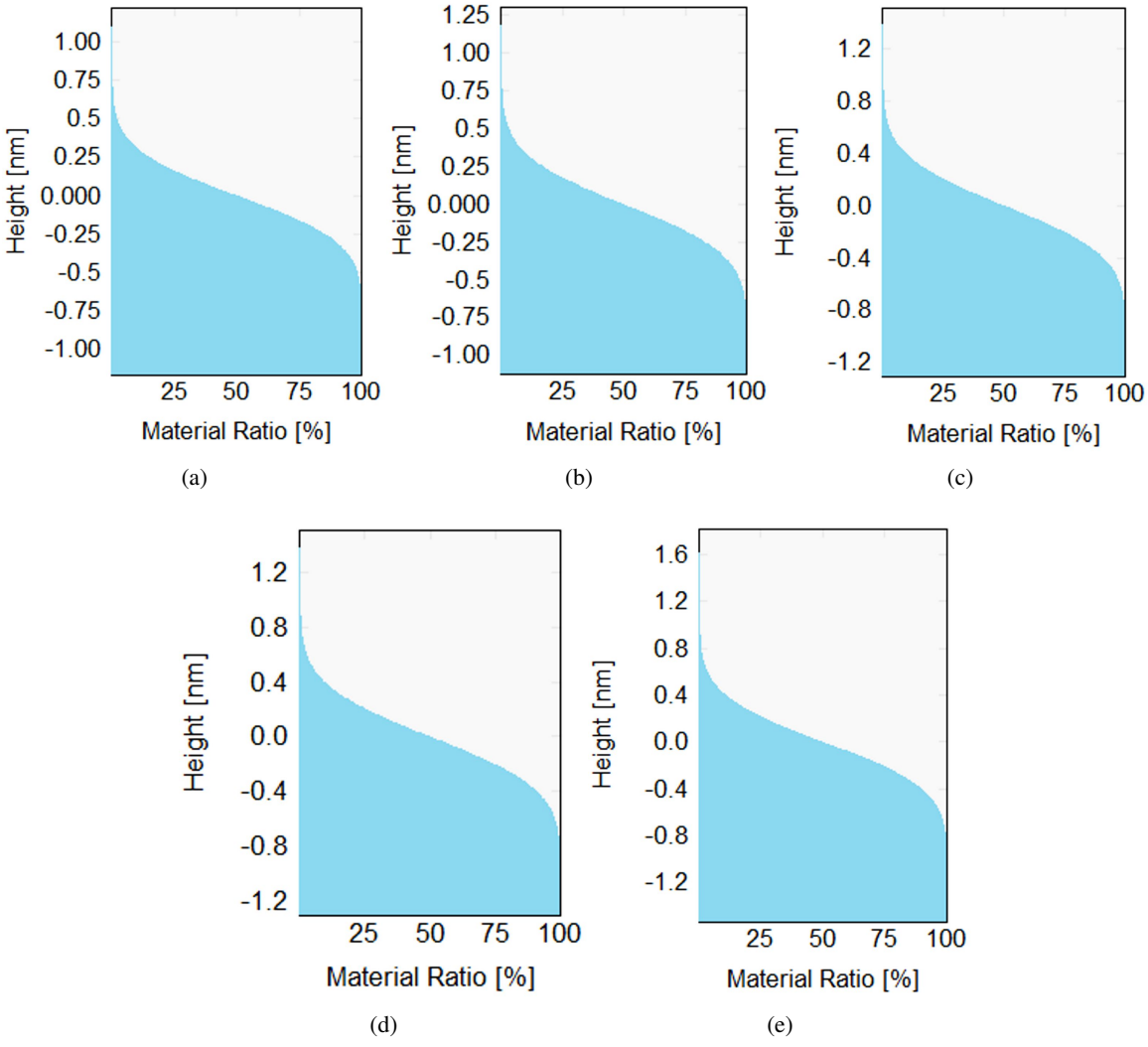

Fig. 5. The Abbott-Firestone curve computed for images of Fig. 1. Sample thickness: (a) 20 nm; (b) 40 nm; (c) 60 nm; (d) 80 nm; (e) 100 nm.

software [29], according to ISO 25178-2:2012 [30] and ASME B46.1-2009 [31]. The height distribution histogram with the integration curve of the histogram computed for images from Fig. 1 is shown in Fig. 4. The height distribution histogram offers information about the flatness of surface. The maximum of the high range is typical of the 100 nm thick film.

Graphical representation of Abbott-Firestone curve computed for images from Fig. 1 is shown in Fig. 5. Mathematically, the bearing ratio curve is a cumulative probability density function of the surface profile height and can be computed by integrating the profile trace [29].

Graphical representation of material probability curve computed for images from Fig. 1 is shown in Fig. 6. The material probability curve is a representation of the material ratio curve, where the heights are plotted in units of standard deviations of a normal (Gaussian) distribution with the same mean and standard deviation as the height data. It is known that a normal distribution of this type of plot is represented by a straight line. This chart is useful in studying how close to a normal distribution is the distribution of heights for the analyzed surface [29].

Isotropic area power spectral density (IAPSD) function computed for images from Fig. 1 is shown

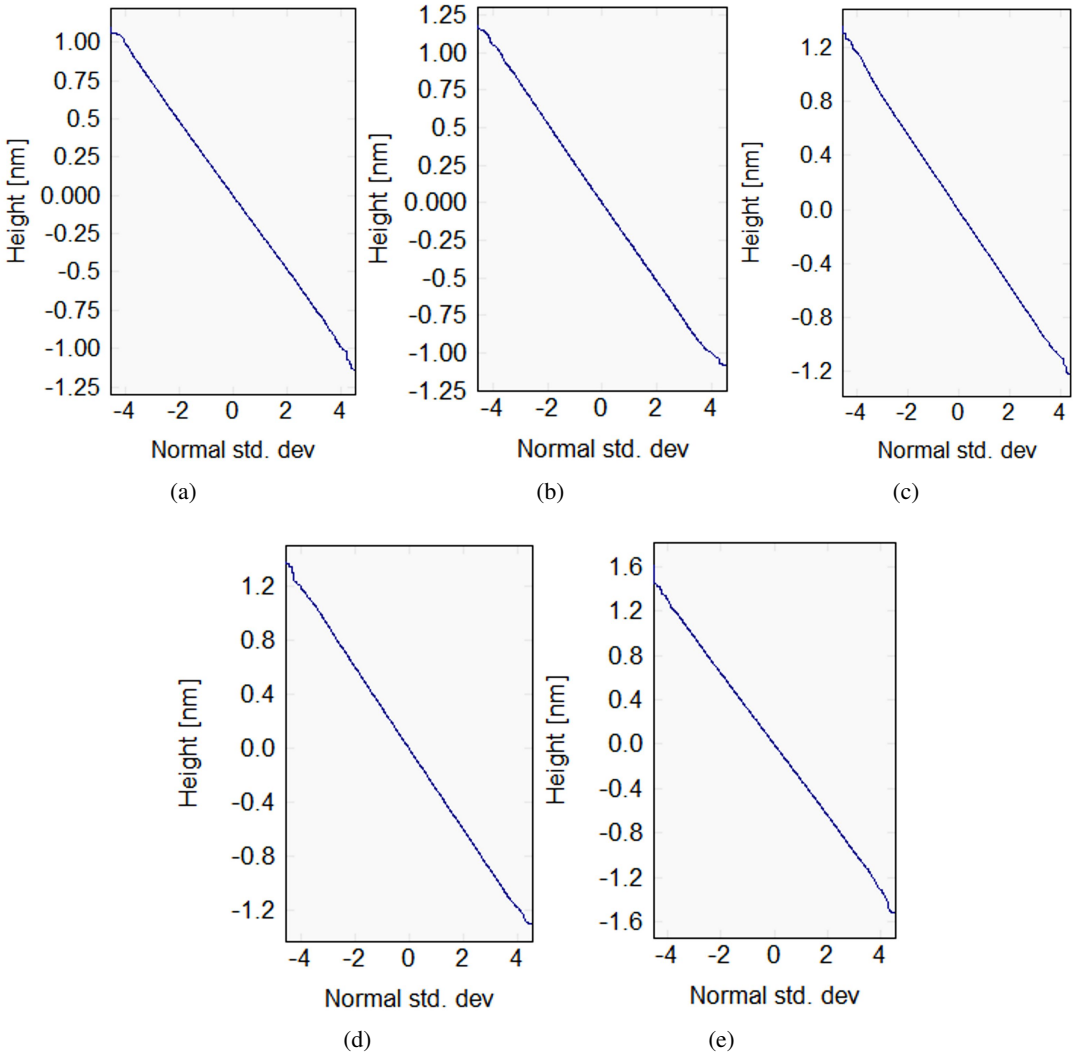

Fig. 6. Material probability curve computed for images of Fig. 1. Sample thickness: (a) 20 nm; (b) 40 nm; (c) 60 nm; (d) 80 nm; (e) 100 nm.

in Fig. 7. The IAPSD function is the area of power spectral density (APSD) function integrated for all angles of given frequencies (inverse wavelength) [29]. This function is similar for all the studied samples.

The integrated radial spectrum function computed for images from Fig. 1 is shown in Fig. 8. According to the calculation, the spectral depths grows for the surfaces of the films with larger thickness.

The fractal dimension, D has been computed for various angles by analyzing the Fourier amplitude spectra for various angles. The amplitude Fourier profile was extracted and the logarithm of frequency and amplitude coordinates were computed. The fractal dimension, D, for each direction was then computed as $D = (6 + s)/2$, where s is the (negative) slope of the log-log curves. The computed fractal dimension is the average for all directions [29]. In Table 1, the values for the fractal dimension, D calculated for the images from Fig. 1 are shown.

In Table 2, statistical parameters of the AFM images, according with ISO 25178-2: 2012 and ASME B46.1-2009 are shown. The value D

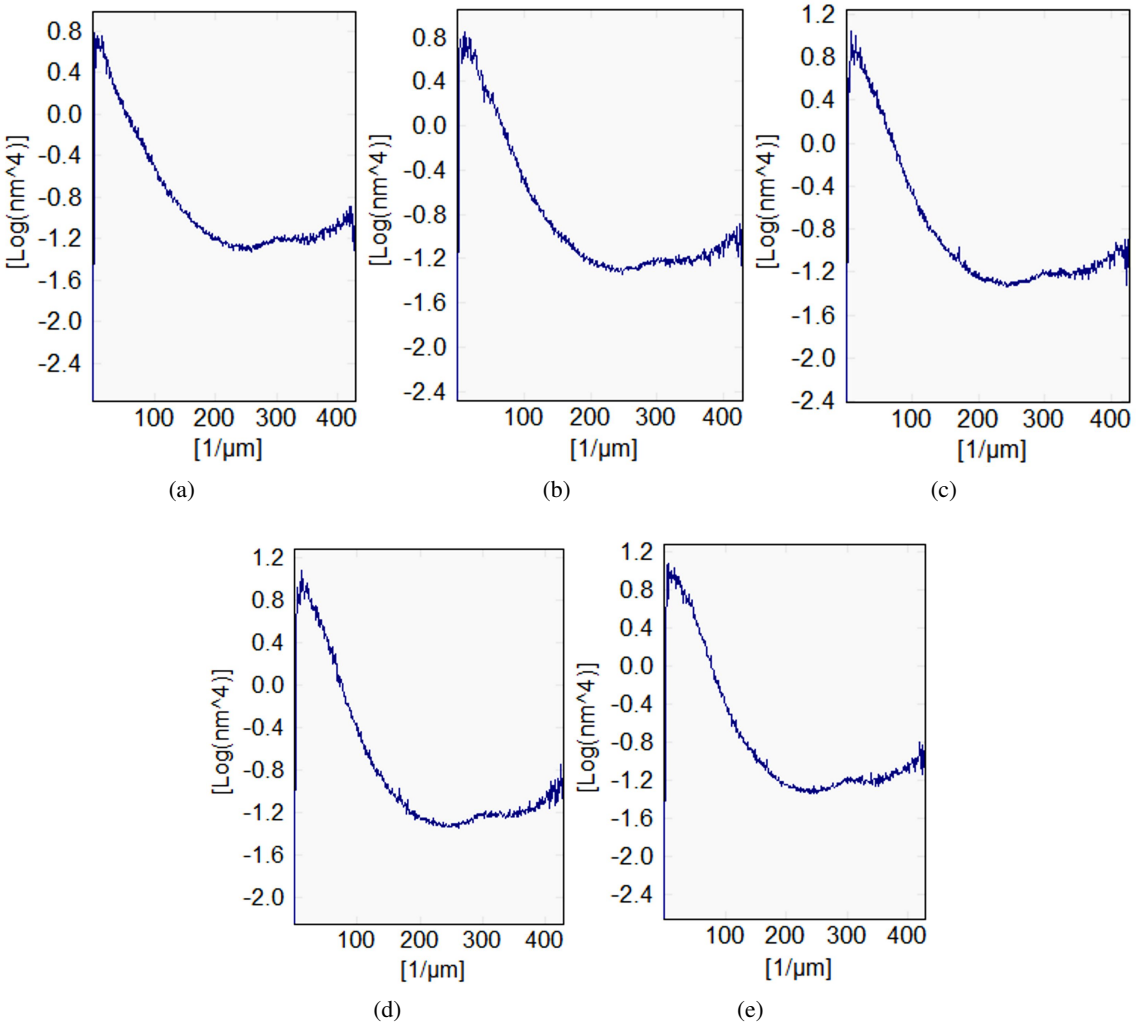

Fig. 7. IAPSD function computed for images from Fig. 1. Sample thickness: (a) 20 nm; (b) 40 nm; (c) 60 nm; (d) 80 nm; (e) 100 nm.

Table 1. The fractal dimension, D, for Ta_2O_5 samples with 20 nm, 40 nm, 60 nm, 80 nm and 100 nm thickness associated with images from Fig. 1.

The fractal	Ta_2O_5 sample thickness				
dimension, D	20 nm	40 nm	60 nm	80 nm	100 nm
Values	2.73±0.01	2.70±0.01	2.68±0.01	2.66±0.01	2.65±0.01

*Statistically significant difference: $P < 0.05$.

systematically decreases with the growth of film thickness. It could be explained by decreasing the amount of features (hills and depths) on the surface. In spite of increasing the numerical values of highs and valleys, the growth of the thickness leads to decreasing of surface irregularity.

The fractal dimension was found to decrease from $D_f = 2.73\pm0.01$ to $D_f = 2.65\pm0.01$ for the thickness increase of 20 nm to 100 nm. The qualitative observations through statistical parameters of the 3-D surface texture revealed that the smoothest surface has been obtained for the sample

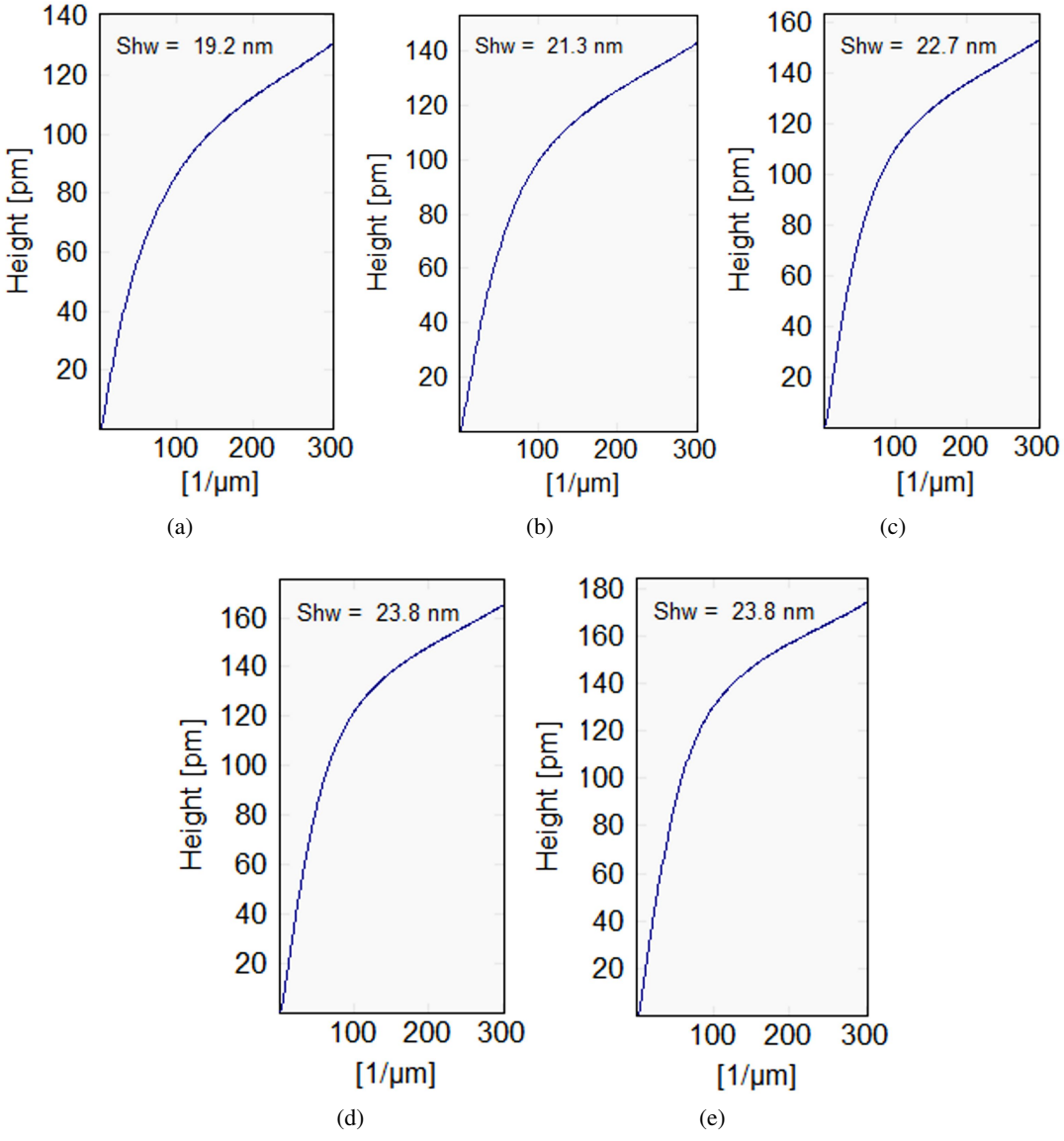

Fig. 8. Integrated radial spectrum function computed for images from Fig. 1. Sample thickness: (a) 20 nm; (b) 40 nm; (c) 60 nm; (d) 80 nm; (e) 100 nm.

with 20 nm thickness (Sa, Sq, Sz, S10z, Sv, Sp have the lower values), while the most irregular topography has been found for the same sample with 20 nm thickness (the fractal dimension D = 2.73±0.01). 1D FFT (fast Fourier transform) line average functions describe Fourier amplitude spectra for each X line or Y column and the corresponding average amplitude spectrum. In our cases, these have been computed for images from Fig. 1 and are shown in Fig. 9.

4. Conclusions

In this study, the correlation between thicknesses of individual Ta_2O_5 thin films and their 3D surface characteristics was analyzed using AFM. We demonstrated that both optical properties and topography of the films change with their thickness as far as quantitative characteristics of surface nanomorphology are concerned. Fractal analysis was used for estimation of texture evolution

Table 2. Statistical parameters according to ISO 25178-2: 2012 and ASME B46.1-2009 for a 1 μm × 1 μm square area of the Ta_2O_5 samples with 20 nm, 40 nm, 60 nm, 80 nm and 100 nm thickness, associated with images from Fig. 1.

Statistical parameters	Symbol	Ta_2O_5 samples				
		20 nm	40 nm	60 nm	80 nm	100 nm
Amplitude parameters						
Arithmetic mean height	Sa [nm]	0.191	0.208	0.222	0.240	0.2536
Root mean square height	Sq [nm]	0.240	0.262	0.279	0.301	0.318
Surface skewness	Ssk [–]	0.022	0.030	0.011	0.019	–0.0001
Surface kurtosis	Sku [–]	3.034	3.021	3.024	3.005	3.033
Maximum height	Sz [nm]	2.276	2.307	2.622	2.694	3.16
Ten point height	S10z [nm]	2.164	2.222	2.467	2.609	2.864
Maximum valley depth	Sv [nm]	1.116	1.127	1.261	1.311	1.543
Maximum peak height	Sp [nm]	1.1	1.180	1.362	1.383	1.617
Hybrid parameters						
Mean summit curvature	Ssc [1/nm]	0.199	0.199	0.199	0.200	0.203
Root mean square gradient	Sdq [–]	0.198	0.198	0.200	0.202	0.206
Area root mean square slope	Sdq6	0.159	0.160	0.162	0.165	0.169
Surface area ratio	Sdr [%]	1.947	1.955	1.985	2.03	2.118
Projected area	S2A [nm^2]	1E+06	1E+06	1E+06	1E+06	1E+06
Surface area	S3A [nm^2]	1E+06	1E+06	1E+06	1E+06	1E+06
Functional parameters						
Surface bearing index	Sbi	0.3425	0.352	0.310	0.340	0.290
Core fluid retention index	Sci	1.578	1.589	1.581	1.575	1.564
Valley fluid retention index	Svi	0.1144	0.111	0.115	0.1128	0.1158
Reduced summit height	Spk [nm]	0.2611	0.2858	0.3092	0.3266	0.3536
Core roughness depth	Sk [nm]	0.6186	0.6731	0.7178	0.7783	0.8184
Reduced valley depth	Svk [nm]	0.2226	0.2357	0.2593	0.2725	0.3013
Spatial parameters						
Density of summits	Sds [$1/\mu m^2$]	3E+04	2.8E+04	2.8E+04	2.6E+04	2.5E+04
Texture direction	Std [°]	15.06	58.61	42.98	7.984	140.8
Texture direction index	Stdi [–]	0.8663	0.8691	0.8497	0.8586	0.8723
Dominant radial wavelength	Srw [nm]	64.19	106.3	144	81.86	181.1
Radial wave index	Srwi [-]	0.2571	0.3235	0.2582	0.2433	0.259
Mean half wavelength	Shw [nm]	19.23	21.28	22.73	23.81	23.81
Correlation length at 20%	Scl20 [nm]	4.942	6.59	6.59	8.237	8.237
Correlation length at 37%	Scl37 [nm]	3.295	4.942	4.942	4.942	4.942
Texture-aspect ratio at 20%	Str20 [–]	0.75	1	1	1	1
Texture-aspect ratio at 37%	Str37 [–]	0.6667	1	1	1	0.75
Cross hatch angle	Sch [°]	54.78	106.5	50.54	10.76	9.388

*Statistically significant difference for all values: $P < 0.05$.

with the film growth. The application of stereometric analysis enabled characterization of topography and evaluation of nanotexture surface parameters. These parameters of the nanoscale films are connected with mechanical stresses caused by lattice mismatch with the substrate. The calculation approach allows numerical estimation of changes caused by growth of the films.

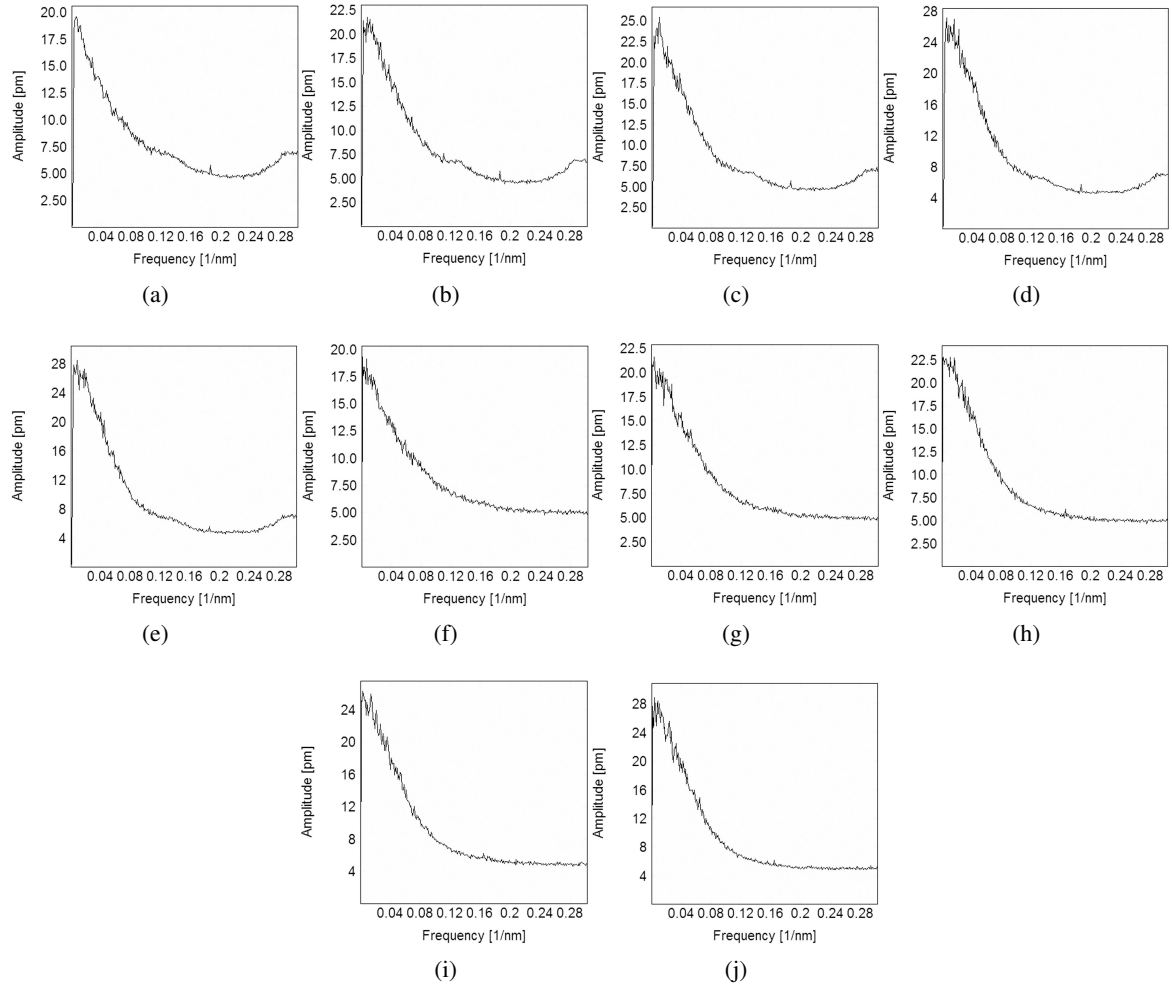

Fig. 9. The average X-Fourier profile, for sample thickness: (a) 20 nm; (b) 40 nm; (c) 60 nm; (d) 80 nm; (e) 100 nm; and the average Y-Fourier profile, for sample thickness: (f) 20 nm; (g) 40 nm; (h) 60 nm; (i) 80 nm; (j) 100 nm.

Acknowledgements

Research described in the paper was financially supported by the National Sustainability Program under Grant LO1401. For the research, infrastructure of the SIX Center was used.

References

[1] ASANO I., NAKAMURA Y., HIRATANI M., NABATAME T., IIJIMA S., SAEKI T., FUTASE T., YAMOMOTO S., SAITO T., SEKIGUCHI T., *Electron. Commun. Jpn.,* 87 (2004), 26.

[2] SIDDIQI M.A., *Dynamic RAM: Technology Advancements,* 1st ed., CRC Press, 2017.

[3] BRANQUINHO R.M.M.S., *Doctoral thesis: Label-free detection of biomolecules with Ta_2O_5-based field effect device,* Universidade NOVA de Lisboa, Portugal, 2012.

[4] ZHANG G., XUE Y., GUO P., WANG H., MA Z.H., *J. Wuhan Univ. Technol.-Mater. Sci. Edit.,* 23 (2008), 632.

[5] SATHASIVAM S., WILLIAMSON B.A.D., KAFIZAS A., ALTHABAITI S.A., OBAID A.Y., BASAHEL S.N., SCANLON D.O., CARMALT C.J., PARKIN I.P., *J. Phys. Chem. C,* 121(1) (2017), 202.

[6] EZHILVALAVAN S., TSENG T.Y., *J. Mater. Sci. Mater. Electron.,* 10 (1999), 9.

[7] YADAV R.P., KUMAR M., MITTAL A.K., PANDEY A.C., *Chaos,* 25 (8) (2015), 083115.

[8] ŢĂLU Ş., STACH S., MAHAJAN A., PATHAK D., WAGNER T., KUMAR A., BEDI R.K., *Surf. Interface Anal.,* 46 (6) (2014), 393.

[9] MÉNDEZ A., REYES Y., TREJO G., STĘPIEŃ K., ŢĂLU Ş., *Microsc. Res. Tech.,* 78 (2015), 1082.

[10] ŢĂLU Ş., BRAMOWICZ M., KULESZA S., SOLAYMANI S., SHAFIKHANI A., GHADERI A., AHMADIRAD M., *J. Indian Eng. Chem.,* 35 (2016), 158.

[11] SHIKHGASAN R., ŢĂLU Ş., DINARA S., SEBASTIAN S., GUSEYN R., *Superlattices Microstruct.,* 86 (2015), 395.
[12] DALLAEVA D., ŢĂLU Ş., STACH S., ŠKARVADA P., TOMANEK P., GRMELA L., *Appl. Surf. Sci.,* 312 (2014), 81.
[13] STACH S., DALLAEVA D., ŢĂLU Ş., KASPAR P., TOMÁNEK P., GIOVANZANA S., GRMELA L., *Mater. Sci.-Poland*, 33 (1) (2015), 175.
[14] KNÁPEK A., SOBOLA D., TOMÁNEK P., POKORNÁ Z., URBÁNEK M., *Appl. Surf. Sci.,* 395 (2017).
[15] ŢĂLU Ş., BRAMOWICZ M., KULESZA S., GHADERI A., DALOUJI V., SOLAYMANI S., FATHI KENARI M., GHORANNEVISS M., *J. Microsc.,* 264 (2016), 143.
[16] ŢĂLU Ş., STACH S., ZAHARIEVA J., MILANOVA M., TODOROVSKY D., GIOVANZANA S., *Int. J. Polym. Anal. Charact.,* 19 (2014), 404.
[17] ELENKOVA D., ZAHARIEVA J., GETSOVA M., MANOLOV I., MILANOVA M., STACH S., ŢĂLU Ş., *Int. J. Polym. Anal. Charact.,* 20 (1) (2015), 42.
[18] ŢĂLU Ş., *Micro and nanoscale characterization of three dimensional surfaces. Basics and applications,* Napoca Star Publishing House, Cluj-Napoca, Romania, 2015.
[19] ARMAN A., ŢĂLU Ş., LUNA C., AHMADPOURIAN A., NASERI M., MOLAMOHAMMADI M., *J. Mater. Sci. Mater. Electron.,* 26 (2015), 9630.
[20] ŢĂLU Ş., STACH S., MENDEZ A., TREJO G., TALU M., *J. Electrochem. Soc.,* 161 (2013), D44.
[21] NASERI N., SOLAYMANI S., GHADERI A., BRAMOWICZ M., KULESZA S., ŢĂLU Ş., POURREZA M., GHASEMI S., *RSC Adv.,* 7(21) (2017), 12923.
[22] KNÁPEK A., SÝKORA J., CHLUMSKÁ J., SOBOLA D., *Microelectron. Eng.,* 173 (2017), 15.
[23] ŢĂLU Ş., MOROZOV I. A., SOBOLA D., ŠKARVADA P., *Bull. Math. Biol.,* 73 (2018), 43.
[24] KNÁPEK A., HORÁČEK M., HRUBÝ F., ŠIKULA J., KUPAROWITZ T., SOBOLA D., *Noise behaviour of field emission cathode based on lead pencil graphite.* In Technical Digest 2017 30^{th} International Vacuum Nanoelectronics Conference (IVNC), Herzogssaal Regensburg, Germany: IEEE, 2017. pp. 274 – 275.
[25] SOBOLA D., ŢĂLU Ş., SADOVSKY P., PAPEZ N., GRMELA L., *Adv. Electr. Electron. Eng.,* 15 (2017), 56.
[26] SOBOLA D., ŢĂLU Ş., SOLAYMANI S., GRMELA L., *Microsc. Res. Tech.,* 80 (12) (2017), 1328.
[27] ŢĂLU Ş., PAPEZ N., SOBOLA D., ACHOUR A., SOLAYMANI S., *J. Mater. Sci.-Mater. Electron.,* 28 (20) (2017), 15370.
[28] GARCZYK Z., STACH S., ŢĂLU Ş., SOBOLA D., WROBEL Z., *JBBBE.,* 31 (2017), 1.
[29] `http://www.imagemet.com`, accessed on: 2018.10.01.
[30] `http://www.iso.org`, accessed on: 2018.10.01.
[31] `https://www.asme.org`, accessed on: 2018.10.01.

Received 2018-10-04
Accepted 2019-04-23